Systematic Errors of Electric Field Measurements in Ferroelectrics by Unit Cell Averaged Momentum Transfers in STEM

Achim Strauch, Benjamin März, Thibaud Denneulin, Mauricio Cattaneo, Andreas Rosenauer, Knut Müller-Caspary

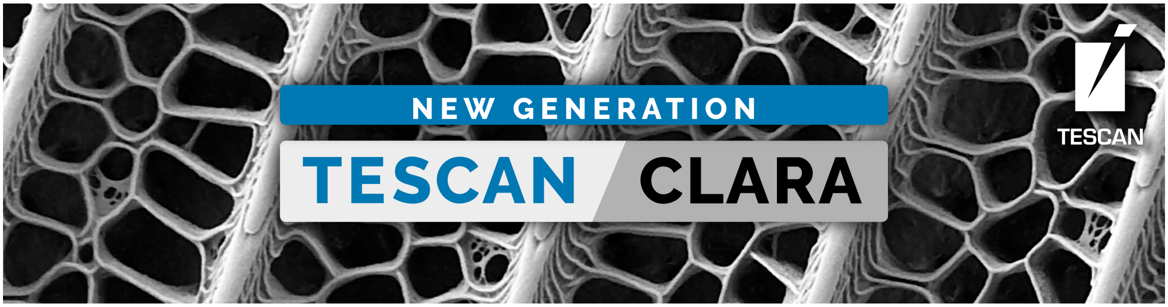

Microscopy and Microanalysis, 2023, **29**, 499–511
https://doi.org/10.1093/micmic/ozad016
Advance access publication 23 February 2023
Original Article

Microscopy AND
Microanalysis

Systematic Errors of Electric Field Measurements in Ferroelectrics by Unit Cell Averaged Momentum Transfers in STEM

Achim Strauch[1,2], Benjamin März[3], Thibaud Denneulin[1], Mauricio Cattaneo[1,2], Andreas Rosenauer[4,5], and Knut Müller-Caspary[1,3,*]

[1]*Ernst Ruska-Centre for Microscopy and Spectroscopy with Electrons, Forschungszentrum Jülich, Jülich 52425, Germany*
[2]*2nd Institute of Physics, RWTH Aachen University, Aachen 52074, Germany*
[3]*Department of Chemistry and Centre for NanoScience, Ludwig-Maximilians-University Munich, Butenandtstr. 11, Germany*
[4]*Institute for Solid State Physics, University of Bremen, Otto-Hahn-Allee 1, Bremen 28359, Germany*
[5]*MAPEX Center for Materials and Processes, University of Bremen, Bibliothekstr. 1, Bremen 28359, Germany*

***Corresponding author:** Knut Müller-Caspary, E-mail: k.mueller-caspary@cup.lmu.de

Abstract

When using the unit cell average of first moment data from four-dimensional scanning transmission electron microscopy (4D-STEM) to characterize ferroelectric materials, a variety of sources of systematic errors needs to be taken into account. In particular, these are the magnitude of the acceleration voltage, STEM probe semi-convergence angle, sample thickness, and sample tilt out of zone axis. Simulations show that a systematic error of calculated electric fields using the unit cell averaged momentum transfer originates from violation of point symmetry within the unit cells. Thus, values can easily exceed those of potential polarization-induced electric fields in ferroelectrics. Importantly, this systematic error produces deflection gradients between different domains seemingly representing measured fields. However, it could be shown that for $PbZr_{0.2}Ti_{0.8}O_3$, many adjacent domains exhibit a relative crystallographic mistilt and in-plane rotation. The experimental results show that the method gives qualitative domain contrast. Comparison of the calculated electric field with the systematic error showed that the domain contrast of the unit cell averaged electric fields is mainly caused by dynamical scattering effects and the electric field plays only a minor role, if present at all.

Key words: 4D-STEM, $BaTiO_3$, electric fields, ferroelectrics, first moment, $PbZr_{0.2}Ti_{0.8}TiO_3$, $SrTiO_3$, unit cell average

Introduction

Due to their promising functionalities in nanoelectronics, ferroelectric materials continue to be an interesting subject for contemporary research (Dawber et al., 2005; Chang et al., 2011; Parker et al., 2016; Carlier et al., 2020; Zhang et al., 2020). One material class are perovskites, for example, $PbZr_xTi_{1-x}O_3$ (Vrejoiu et al., 2006; Jia et al., 2007; Karthik et al., 2012; Copie et al., 2017; Denneulin et al., 2018; Pintilie et al., 2020; Ma et al., 2021; Vandana et al., 2021; van der Veer et al., 2021; Beklešovas et al., 2022; Chen et al., 2022) and $BaTiO_3$ (BTO) (Everhardt et al., 2020; Xu & Li,2020; Wei et al., 2021; Denneulin & Everhardt, 2022; Meng et al., 2022; Ferrero et al., 2023). There are a wide range of devices in the field of information technology that can be built with ferroelectric components, for example, capacitors (Shin, 2019), tunnel junctions (Wen et al., 2013; Garcia & Bibes, 2014; Ding et al., 2021), high electron mobility transistors (Zhao et al., 2021), and spintronics applications (Tao & Tsymbal, 2021). Therefore, a detailed understanding of structural, and particularly, electrical properties of ferroelectrics at the nanoscale is needed to design and characterize such devices.

Ferroelectrics have a spontaneous electric polarization leading to surface charges and a nonzero electric field (electric depolarization field) in the material in finite systems. Depending on the size of the material, domain formation with different polarizations becomes energetically favorable. The coercive electric field is the external field that must be applied to reduce the average electric field in the material to zero. Often, switching experiments are done to measure the properties of ferroelectrics including the coercive electric field by contacting with electrodes and applying alternating fields (Parker et al., 2016; Shin, 2019). However, this type of experiment does not provide information about the behavior on the nanoscale. Piezoresponse force microscopy could give informations down to several nanometers but not at the unit cell scale (Gruverman & Kalinin, 2006; Gruverman et al., 2019; Kwon et al., 2020). Electron microscopy is a promising imaging solution to close this methodological gap as electrons can be used to probe electric fields down to atomic resolution in a transmission electron microscope.

To this end, several methods are in general feasible, such as electron holography (Lichte, 1986, 1991, 1993, 2008; Lichte et al., 1996, 2002; Lichte & Lehmann, 2008; Denneulin et al., 2018; Haas et al., 2019; McCartney et al., 2019) or differential phase contrast (DPC) and first moment (FM) imaging (Lohr et al., 2012, 2015; Shibata et al., 2012; Lubk & Zweck,2015; MacLaren et al., 2015; Shibata et al., 2015; Müller-Caspary et al., 2017, 2019*b*). Common to those

Received: September 15, 2022. **Revised:** December 9, 2022. **Accepted:** January 25, 2023

methodologies is the capability of measuring the electrostatic potential (McCartney et al., 1994; Yazdi et al., 2015; Lazić et al., 2016; Lazić & Bosch, 2017; Shibata et al., 2017; Yücelen et al., 2018), the electric fields (Frabboni et al., 1987; Deguchi et al., 2010; Bauer et al., 2014; Close et al., 2015), or the charge density (Voelkl et al., 2019) under certain conditions. As to FM imaging via scanning transmission electron microscopy (STEM), the introduction of ultra-fast cameras (Ballabriga et al., 2011; Müller et al., 2013; Plackett et al., 2013; Müller-Caspary et al., 2015; Ryll et al., 2016; Tate et al., 2016) enabled the recording of four-dimensional STEM (4D-STEM) data with full momentum resolution. In particular, the average in-plane momentum transferred to the electron beam (Waddell & Chapman, 1979; Müller et al., 2014) via interaction with the specimen gives, in principle, access to electric fields within the interaction volumes defined by the position and extension of the STEM probe (Müller et al., 2014; Müller-Caspary et al., 2018; Gao et al., 2019; Beyer et al., 2021). Subsequently, charge densities and electrostatic potentials can be mapped via postprocessing techniques. Important prerequisites for the direct mapping of electric fields at the atomic scale have been worked out in former studies and mainly involve the requirement of ultrathin specimens.

With regard to thicker specimens with polarization-induced electric fields superimposed on the atomic ones, symmetry assumptions have been made, under which meso-scale electric fields can be mapped from FM STEM data averaged across unit cells (Müller-Caspary et al., 2019*a*). Importantly, this methodology comes along with systematic errors (Müller-Caspary et al., 2019*a*; Campanini et al., 2020; Grieb et al., 2021) arising from symmetry breakings and dynamical scattering, to be studied material- and case-dependent by detailed accompanying simulations.

In hypothetical monodomain ferroelectrics, the presence of rather strong polarization-induced electric fields would be expected. However, even in such cases it must be taken into account that free charges are attracted by the surface charges of the ferroelectric. This leads to a screening field that counteracts the depolarization field to a large extent reducing the averaged electric field in the ferroelectric by a few orders of magnitude (Kalinin et al., 2018). As will be demonstrated in this work, different ferroelectric domains are straight forwardly distinguishable by unit cell averaged FMs. The question to which extent this contrast can be related to the relatively weak remaining electric fields, or whether it arises from systematic errors, therefore appears highly relevant for future characterizations of ferroelectric nanostructures by STEM.

In this work, the influence of dynamical scattering on the unit cell averaged FM caused by atom displacements, specimen thickness, crystallographic tilt, acceleration voltage, semi-convergence angle, and bonding effects is investigated. This is done in both simulations and experiments. The systematic error of a FM-based electric field calculation is quantified in a variety of case studies, and the reliability as well as feasibility of polarization mapping with this method are addressed. Since the focus is on the systematic error, the presented simulations do not contain polarization-induced electric fields explicitly—taking into account the actual field distribution in ferroelectrics in simulations in the presence of domains is left as a future task.

Initially, the concept for calculating long-range electric fields from unit cell averaged momentum transfers recorded under atomic resolution STEM settings is summarized. In particular, the physical origin of systematic errors in this method is explained. Next, the used materials [$SrTiO_3$ (STO), BTO, and $PbZr_{0.2}Ti_{0.8}TiO_3$ (PZT)] and the experimental setups are presented. Besides the established ferroelectrics BTO and PZT, the nonferroelectric material STO is considered in experiments and simulations as well, because any internal electric field can be ruled out, facilitating the study of systematic errors in pure form. In the ferroelectric cases, focus lies on inherent variations of systematic errors across domain boundaries. After this, the impacts of atom displacements, specimen thickness and tilt, acceleration voltage, semi-convergence angle, and bonding effects are investigated in a simulation study. Several experiments were then conducted using a variety of settings, and these were compared to simulations using the same parameters.

Theory

Using Ehrenfest's theorem (Ehrenfest, 1927), a relation between the in-plane-momentum transfer $\vec{p}_\perp$ and the in-plane electric field $\vec{E}_\perp$ can be given as

$$d\langle \vec{p}_\perp \rangle = -e\langle \vec{E}_\perp \rangle\, dt \tag{1}$$

with the time t that the electron travels through the electric field, the elementary charge e and sharp brackets representing expectation values. Using the paraxial approximation, dt can be replaced with dz/v with the distance z along the optical axis and the speed v of the electrons. Inserting this in equation (1) yields (Müller et al., 2014)

$$d\langle \vec{p}_\perp \rangle = -\frac{e}{v}\langle \vec{E}_\perp \rangle\, dz. \tag{2}$$

Integrating along the specimen thickness Δz results in

$$\langle \vec{p}_\perp \rangle = -\frac{e}{v}\int_0^{\Delta z} \langle \vec{E}_\perp \rangle\, dz. \tag{3}$$

The expectation value of the in-plane electric field is given by

$$\langle \vec{E}_\perp \rangle = \iint \vec{E}_\perp(x, y, z) I(x, y, z)\, dy\, dx \tag{4}$$

with the intensity I of the electron beam in the specimen.

The expectation value of the in-plane momentum transfer is given by

$$\langle \vec{p}_\perp \rangle = \iint \vec{p}_\perp(p_x, p_y) I(p_x, p_y)\, dp_x\, dp_y, \tag{5}$$

where the intensity $I(p_x, p_y)$ in diffraction space is recorded by a calibrated pixelated detector on which $\vec{p}_\perp = (p_x, p_y)$ is the coordinate of a pixel.

As soon as dynamical scattering plays a major role, the momentum transfer is not related to the electric field by a simple expression anymore. If the electric field in the sample and the illumination are known, the momentum transfer can be easily calculated by a multislice approach. However, inverting this problem, i.e., starting from recorded diffraction patterns $I(p_x, p_y)$, would need an iterative process. This is a promising field of research, however, a simpler and direct approach would be desirable.

The electric field can be separated in the following way:

$$\vec{E}_\perp = \vec{E}_{\perp,\mathrm{atom}} + \vec{E}_{\perp,\mathrm{ext}} \tag{6}$$

with atomic electric fields $\vec{E}_{\perp,\mathrm{atom}}$ and external fields $\vec{E}_{\perp,\mathrm{ext}}$. External, in this context, means that the field can be regarded constant across a unit cell. Assuming the external electric field $\vec{E}_{\perp,\mathrm{ext}}$ to be constant also across the sample thickness leads to

$$\int_0^{\Delta z} \langle \vec{E}_{\perp,\mathrm{ext}} \rangle \, dz = \vec{E}_{\perp,\mathrm{ext}} \cdot \Delta z. \tag{7}$$

Combining equations (3), (6), and (7) gives

$$\vec{E}_{\perp,\mathrm{ext}} + \frac{1}{\Delta z} \int_0^{\Delta z} \langle \vec{E}_{\perp,\mathrm{atom}} \rangle dz = -\frac{v \cdot \langle \vec{p}_\perp \rangle}{e \cdot \Delta z}. \tag{8}$$

Notably, only the atomic contributions involve electric fields that vary at the scale of the STEM probe. This is one reason why momentum transfer and electric field lose their proportional relationship at elevated specimen thickness. However, assuming a centrosymmetric scattering geometry, the momentum transfers of opposite scan points with respect to the symmetry center cancel out each other exactly, irrespective of dynamical scattering effects. Consequently, an average of the field across a unit cell would be zero.

In the following, the average over all scan points in a unit cell is denoted with a bar. Applying this unit cell average to equation (8) assuming a centrosymmetric unit cell and no mistilt leads to

$$\vec{E}_{\perp,\mathrm{ext}} = -\frac{v \cdot \overline{\langle \vec{p}_\perp \rangle}}{e \cdot \Delta z}. \tag{9}$$

However, ferroelectrics such as BTO and $\mathrm{PbZr}_x\mathrm{Ti}_{1-x}\mathrm{TiO}_3$ having noncentrosymmetric unit cells as the energetically ground state prefer an atom shift away from the symmetric positions. In fact, that is the origin of the polarization. Additionally, mistilts from a desired zone axis can also lead to noncentrosymmetric scattering geometries in centrosymmetric crystals. In these cases, the unit cell average of equation (8) takes the form

$$\vec{E}^a := \vec{E}_{\perp,\mathrm{ext}} + \vec{\delta} = -\frac{v \cdot \overline{\langle \vec{p}_\perp \rangle}}{e \cdot \Delta z}. \tag{10}$$

Here, the apparent electric field $\vec{E}^a$ was defined, being composed of the external electric field to be measured ideally, and a systematic error

$$\vec{\delta} := \frac{1}{\Delta z} \overline{\int_0^{\Delta z} \langle \vec{E}_{\perp,\mathrm{atom}} \rangle \, dz} \tag{11}$$

caused by dynamical scattering effects in combination with the violation of centro-symmetry (Müller-Caspary et al., 2019*a*).

Material/Experimental Setup and Simulation Details

STO, BTO, and PZT were investigated in the simulation study. The unit cells are shown in Figure 1. STO and PZT were also investigated in experiments. Therefore, a sample was used that had been characterized by Denneulin et al. (2018) before. The sample was prepared with a dual beam FIB/SEM FEI Helios and further thinned by a nanomill. STO was used as a reference case as it does not have polarization effects. As PZT shows polarization effects above 4 nm thickness (Jia et al., 2006; Gao et al., 2017), it was used in the polarization case. The sample was investigated in two different setups, an FEI TITAN STEM 80-300 (Titan-S) (Heggen et al., 2016) with a Medipix Merlin detector (Plackett et al., 2013) and an FEI Titan G^2 60-200 (ChemiSTEM) with an electron microscope pixel array detector (EMPAD) (Tate et al., 2016) detector.

For the simulations, the software STEMsim (Rosenauer & Schowalter, 2008) was employed. The crystal was set up with periodic boundary conditions. Hence, there were no surface charges included preventing the appearance of any external field caused by polarization. The electrostatic potential of the crystal was calculated in an isolated atom model (IAM) using a look up table (Lobato & Dyck, 2014) for the scattering amplitudes of isolated atoms. With these conditions, any nonzero value in the unit cell averaged electric field is caused by dynamical scattering effects and, hence, is a systematic error. With the crystal potential, a multislice calculation (Cowley & Moodie, 1957, 1959) was done with a slice thickness of one unit cell. The simulation resulted in an intensity distribution in diffraction space, from which the FM was calculated. Inserting zero for the external field in equation (10) gives for the systematic error:

$$\vec{\delta} = -\frac{v \cdot \overline{\langle \vec{p}_\perp \rangle}}{e \cdot \Delta z}. \tag{12}$$

For a density functional theory (DFT) calculation, WIEN2k (Blaha et al., 2020) was used. The calculation was set up using the known literature values for BTO and a self-consistency cycle (SCF) cycle was run. From the result, the X-ray form factors were calculated with the sub-routine LAPW3. The electron scattering form factors were calculated with the Mott-Bethe formula (Bethe, 1930; Mott, 1930) and imported into STEMsim using the modified atomic scattering amplitudes (MASA) model (Rosenauer et al., 2005; Müller et al., 2010).

Results

Simulation Study

For the probe, an acceleration voltage of 300 kV was used and the semi-convergence angle was set to 25 mrad. All aberrations were set to zero. In the following cases, only one parameter of the simulation was varied at a time.

In the first simulation series, the calculation was performed for different atom displacements from the symmetry position to study the impact of the degree of symmetry breaking on the systematic error δ. In one case, the atom displacements were set according to the literature values (Kwei et al., 1993; Frantti et al., 2000; Leal et al., 2009). The parameter d was introduced to scale the displacements to artificial magnitudes. In particular, $d = 0$ corresponds to no displacement from the symmetry position, $d = 1$ to the displacement given in the literature, and $d = 2$ refers to a displacement twice as large as in the literature.

The results are shown in Figure 2. For zero atom displacements, meaning that the unit cell is centrosymmetric, the systematic error is also zero, as expected. For all other cases, the thickness dependence of the systematic error has a complicated behavior with a few general features. The systematic error is already nonzero in very thin specimens with thicknesses above 1 nm. In the first few nanometers, the systematic error increases up to the order of 10 MV/cm. For large thicknesses, the systematic error shows a slow convergence but not necessarily to zero in the order of 1 MV/cm for BTO and 10 MV/cm for PZT. In between, the behavior is more random. In general, the systematic error increases with increasing atom displacements. This cannot only be seen from the behavior for different displacements but also from the larger systematic error in

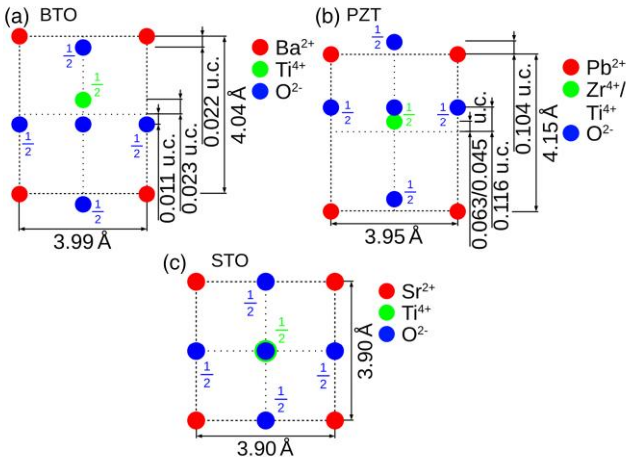

Fig. 1. The unit cells of (**a**) BTO, (**b**) PZT, and (**c**) STO in projection view with the respective literature values (Kwei et al., 1993; Frantti et al., 2000; Leal et al., 2009) for the unit cell size and the atom displacements. The 1/2 denotes atom sites that are not at the front side of the unit cell but shifted half a unit cell to the back. For illustration, the sizes are not to scale.

PZT compared to BTO that is due to the larger displacements in PZT. For small displacements in BTO, the systematic errors adopt values up to 3 MV/cm, where approximately 25 MV/cm are reached in PZT. Because of the complicated thickness dependence, this trend is not observed at some particular thickness values (e.g., 18 nm in BTO or 12 nm in PZT). As can be seen in the position-averaged convergent-beam electron diffraction (PACBED) data, the effect of dynamical scattering on the intensity distribution is not obvious for BTO, whereas intensity redistributions in the PACBED can be seen by eye for PZT at 40 nm thickness at realistic displacements ($d = 1$) already.

In the following part, the displacement is set to literature values ($d = 1$) and several parameters of the microscope are varied to ascertain whether they can reduce the systematic error. In the next simulation series, the influence of the acceleration voltage is investigated as shown in Figure 3. In general, the systematic error decreases with increasing acceleration voltage. For example in PZT, the error reaches 15 MV/cm for 300 kV and 35 MV/cm for 60 kV at a thickness of around 3 nm. Additionally, this trend is violated at some thicknesses (especially in PZT in the range from 30 to 50 nm). Although increasing the acceleration voltage reduces the impact of dynamical scattering, no simple way for minimizing δ is obvious within the range of electron energies covered by this simulation.

In addition, the influence of the semi-convergence angle was investigated as depicted in Figure 4. In general, the systematic error decreases with increasing semi-convergence angle. In PZT, the error reaches 15 MV/cm for 25 mrad and 150 MV/cm for 2 mrad at thicknesses below 10 nm, respectively. Again, this trend is violated for some thicknesses. It is important to note that, for the small convergence angles, no atomic resolution is obtained that could give rise to a unit cell averaging procedure in experimental data sets. These data were included as it provides insights into the accuracy of studying ferroelectrics by nano-beam electron diffraction.

Only the IAM was used up to this stage of the analysis. To check the influence of bonding on the systematic error, a DFT calculation in BTO was performed using the WIEN2K software. The result is shown in Figure 5 where it can be observed that differences to the IAM start at around 10 nm. These differences become more pronounced in the range from 40 to 55 nm as the factor between the two models expands and becomes negative (IAM almost 0 MV/cm and the DFT model around −0.5 MV/cm). Generally, bonding is a minor effect compared to the ionic displacements dealt with above.

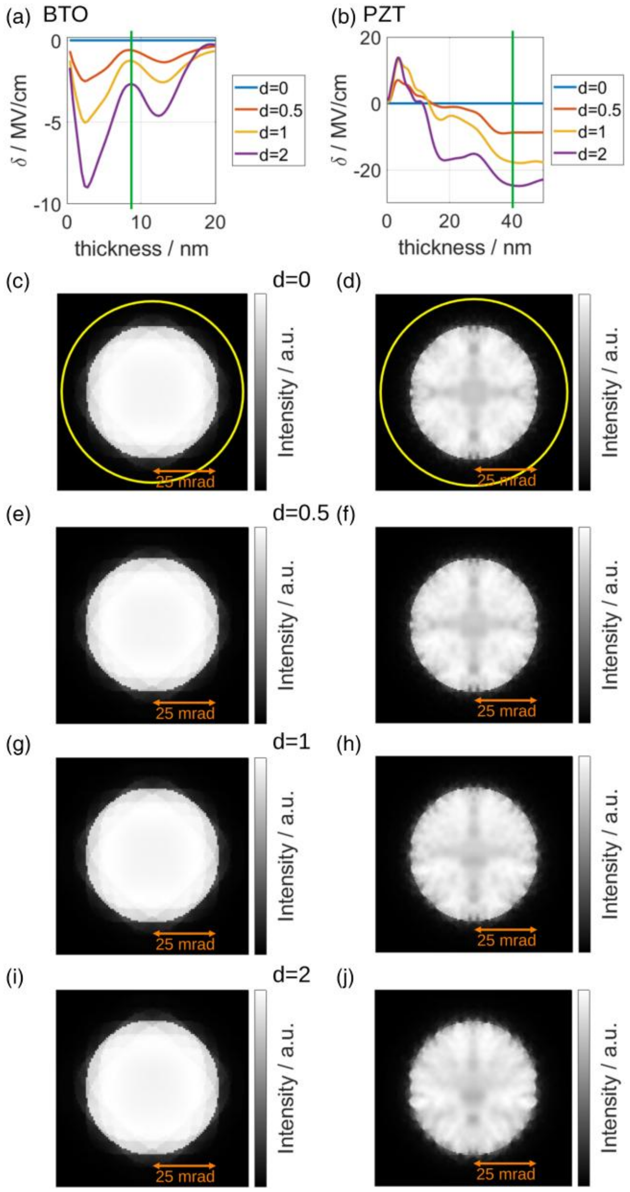

Fig. 2. Influence of specimen thickness and atom displacements on the systematic error δ in (**a**) BTO and (**b**) PZT. The atom displacement d is normalized to the literature values (Fig. 1) of the corresponding material. With $d = 0$, the atoms are at the symmetry positions, $d = 1$ denotes shifts to the positions from the literature. Note that this results in larger absolute displacements in PZT compared to BTO for the same d-values. For the thicknesses of 9 and 40 nm marked with a vertical green line, the PACBEDs are shown in (**c**)–(**j**), BTO in the left, PZT in the right column. The size of the virtual CoM-detector is marked with a yellow cycle in (**c**) and (**d**).

In an experiment, the sample should be in zone axis, but nevertheless mistilts in the range of a few milliradians can easily occur. Hence, the influence of sample tilt on the systematic

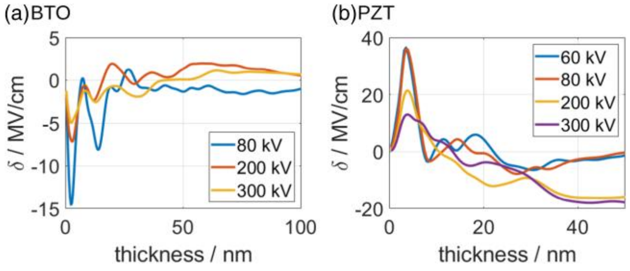

Fig. 3. Influence of sample thickness and high tension of the microscope on the systematic error δ in (**a**) BTO and (**b**) PZT with $d = 1$ (i.e., cation displacements from the literature).

error was investigated in the next simulation series as shown in Figure 6. Tilt out of zone axis introduces a systematic error parallel to the tilt direction even in STO, a material that is centrosymmetric and would not create a net deflection by polarization-induced electric fields in theory. This effect can also be seen if tilting BTO or PZT perpendicular to the polarization axis. If tilting parallel to the polarization axis, the systematic error that is already present changes significantly. In BTO, this effect is even one magnitude larger than the dynamical scattering effect for a tilt of only 1 mrad. As a general observation, the systematic error arising from mistilt increases with the tilt angle and this is observed for almost all thicknesses.

In conclusion, besides the dependence on specimen thickness, the mistilt from zone axis appears to be the most relevant source of error in real experiments. In fact, systematic errors are already large for mistilts within the typical range of precisions that can be achieved by manually aligning the specimen. Moreover, specimens are bent within the field of view very often, introducing a locally varying systematic error $\vec{\delta}$ that could easily be misinterpreted as a variation of electric fields in the specimen, especially if the tilt changes abruptly across domain boundaries. To uncover the impact of experimental uncertainties and the geometry of real specimens, we conducted a comprehensive experimental study.

Experimental Study

For the experiments, several 4D-STEM scans have been performed under different conditions. The experimental conditions are summarized in Table 1 for two PZT cases and STO, where numerous further data were analyzed as shown in the Supplementary Material. All datasets are from the same sample but from different regions. To calibrate position and size of the Ronchigram on the detector, a circle was fitted by radial gradient maximization (Müller et al., 2012). The momentum transfer was calculated according to equation (5) where the relative rotation between the scan coordinate system and the detector has been taken into account. Because long-range electric fields from potential residual depolarization fields, charged contamination, and the environment of the microscope cannot be ruled out completely and could shift the Ronchigram, using its center to define the zero point of the momentum transfer is often inaccurate. As scans PZT 2 and STO contain a vacuum region, it can be used to define the zero point, i.e., $\langle \vec{p}_\perp \rangle = 0$.

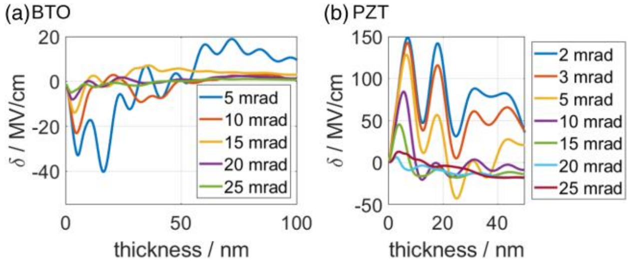

Fig. 4. Influence of sample thickness and semi-convergence angle of the electron probe on the systematic error δ in (**a**) BTO and (**b**) PZT with $d = 1$ (i.e., cation displacements from the literature).

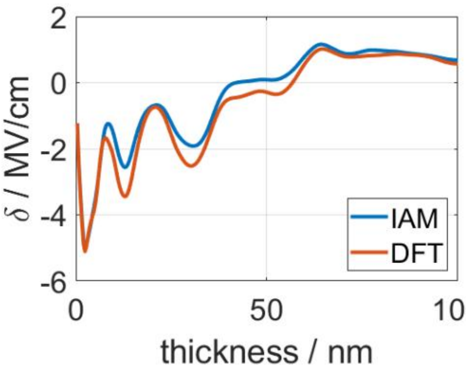

Fig. 5. Influence of sample thickness and atom model on the systematic error δ in BTO. The calculation was done once with the IAM and once with the electron density from DFT calculations.

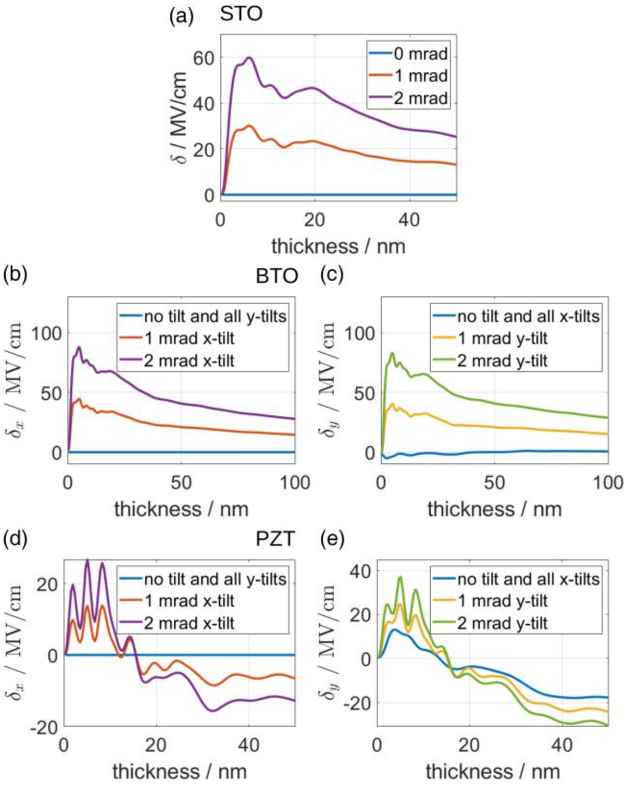

Fig. 6. Influence of sample thickness and sample tilt on the systematic error δ in (**a**) STO, (**b**,**c**) BTO, and (**d**,**e**) PZT. In STO, the tilt was done on the main crystal axis 〈100〉. The systematic error arises on the same axes and is zero for the component perpendicular to it. On the other materials, the tilt was done perpendicular to the polarization axis (*x*-tilt) and parallel to it (*y*-tilt).

Table 1. Experimental Parameters Used for the 4D-STEM Experiments with the Acceleration Voltage U, Semi-convergence Angel α, Scan Area in Scan Points S, Detector Pixel D, Dwell Time per Scan Point t_{dw}, and Dead Time per Scan Point t_{de}.

Scan	PZT 1/PZT 2	STO
Material	PZT	STO
Setup	ChemiSTEM	Titan-S
U (kV)	200	300
α (mrad)	24.6	22.6
S	128×512	255×2048
D	128×128	256×256
t_{dw} (ms)	1	1
t_{de} (ms)	1	0

PZT 1 does not contain a vacuum region to define the origin in momentum space. To remove arbitrariness, the zero point is chosen as the mean value in one domain. That is the upper domain, as shown in Figure 8. Consequently, momentum transfers are then approximately zero across the reference domain region, and the momentum transfers in adjacent domains are to be interpreted relative to the reference one. The consequences of this procedure are depicted in Figure 7 for the ideal situation. In that case, the outer domains would show a mean momentum transfer of zero and the inner domain a mean momentum transfer in the diagonal direction, if the deflection corresponded to a real electric field.

Another solution to the problem of a lacking vacuum region in the scan itself would be to fit the Ronchigram position in a vacuum reference scan performed separately after removing the specimen from the field of view. However, this procedure turned out to yield ambiguous results, especially unexpected global offsets of the measured $\langle \vec{p}_\perp \rangle$ in the region of interest that almost completely overshadowed the variations of the momentum transfer due to the local specimen properties. In that respect, the following factors could be identified as possible sources of this effect. First, moving the sample (and with it the holder including stage) changes the electrical environment, which can lead to a different background electric field. Second, the position of the diffraction pattern might change slightly after, e.g., blanking the beam between two scans. Consequently, relative momentum transfer between domains was focussed on, assuring locality of the interpretation of $\langle \vec{p}_\perp \rangle$.

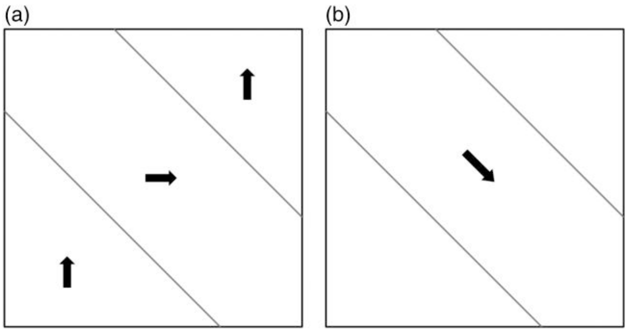

Fig. 7. Polarization in a ferroelectric with 45° domain boundaries. (**a**) Polarization if the zero point is known. (**b**) Polarization if the zero point is defined by the mean value of the outer domain.

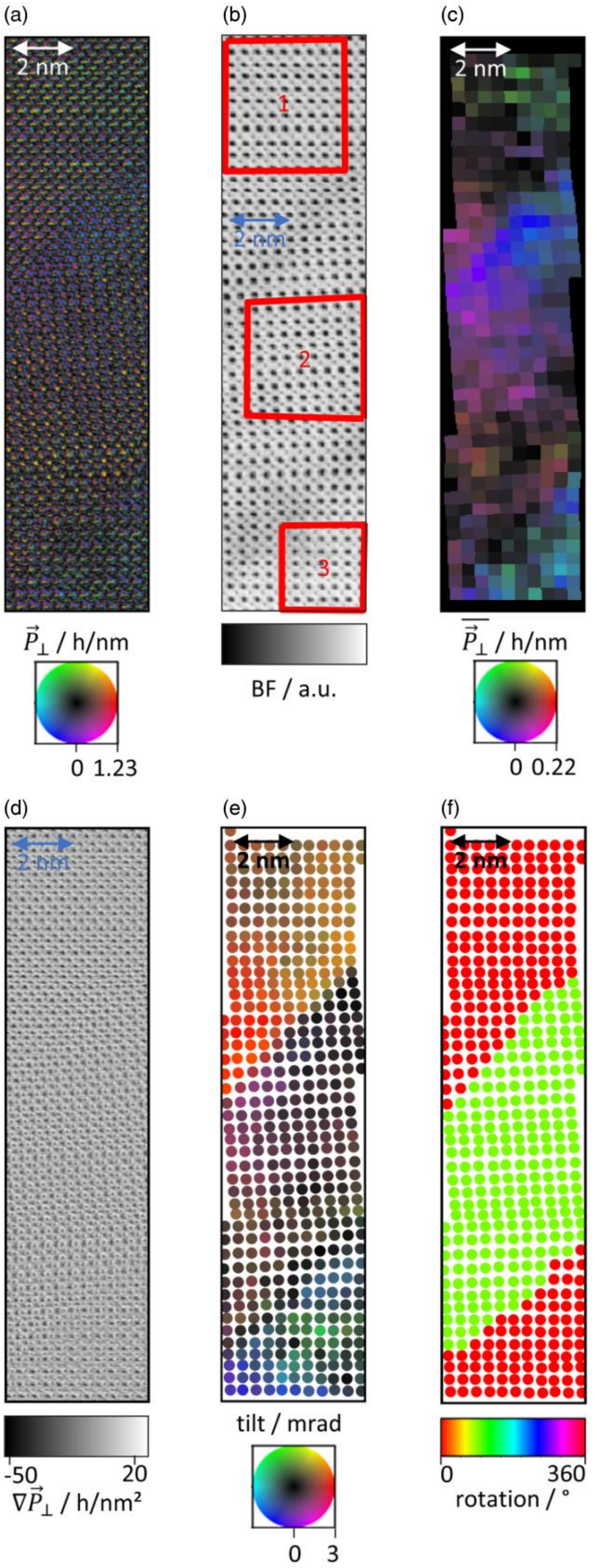

Fig. 8. Experimental results from PZT 1. (**a**) FM. (**b**) BF image with the evaluation regions marked with red rectangles. (**c**) Unit cell average of (a). (**d**) Divergence of (a). (**e**) Tilt map. To visualize small variations, outliers were truncated. The signal to noise ratio was good enough for a unit cell precise fitting. (**f**) In-plane rotation. The relative rotation between the upper/lower and the middle domain is 92.2°. The axis of the images correspond to the main crystallographic axis.

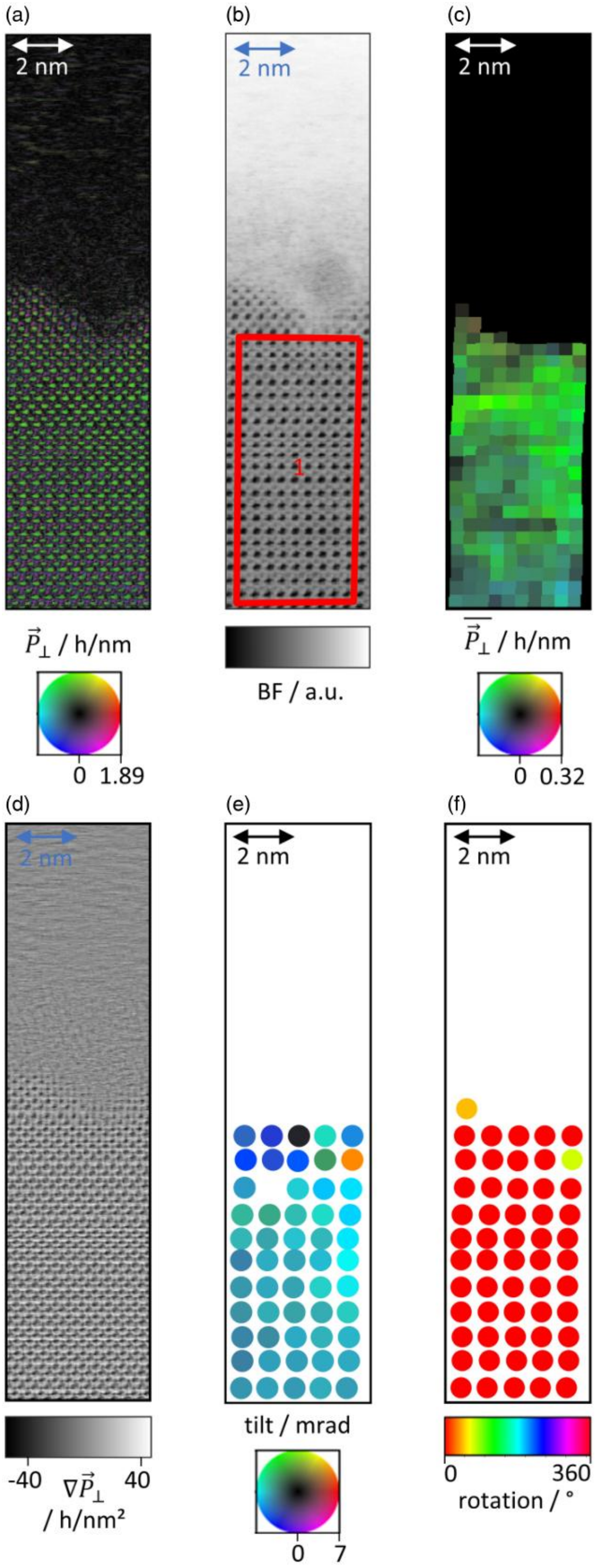

Fig. 9. Experimental results from PZT 2. (**a**) FM. (**b**) BF image with the evaluation region marked with a red rectangle. (**c**) Unit cell average of (**a**). (**d**) Divergence of (**a**). (**e**) Tilt map. To improve the signal to noise ratio, averaging across two by two unit cells was necessary. Please note that the signal to noise of the Kikuchi lines in the top two lines was still weak resulting in a large fitting error. Therefore, the values in the top two lines should not be trusted. To visualize small variations, outliers were truncated. (**f**) In-plane rotation. The axis of the images correspond to the main crystallographic axis.

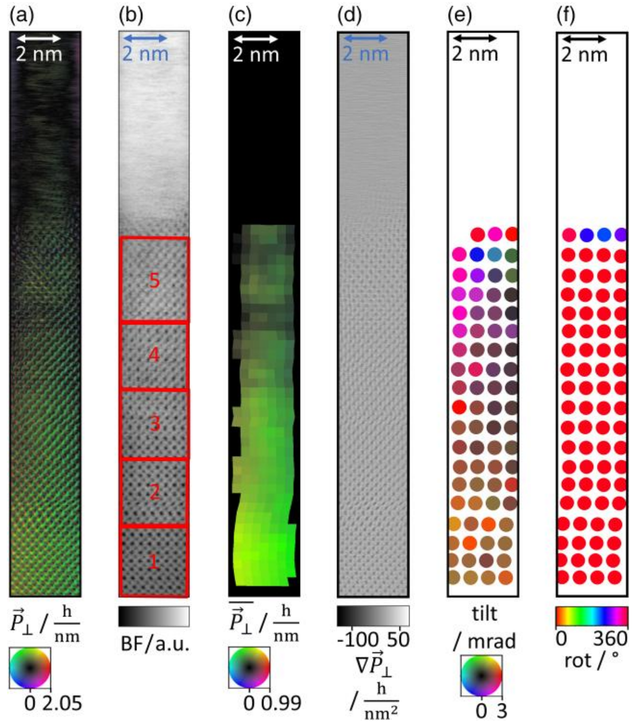

Fig. 10. Experimental results from STO. (**a**) FM. (**b**) BF image with the evaluation regions marked with red rectangles. (**c**) Unit cell average of (**a**). (**d**) Divergence of (**a**). (**e**) Tilt map. To improve the signal to noise ratio, averaging across two by two unit cells was necessary. Please note that the signal to noise of the Kikuchi lines in the top two lines was still weak resulting in a large fitting error. Therefore, the values in the top two lines should not be trusted. To visualize small variations, outliers were truncated. (**f**) In-plane rotation rot. The axis of the images correspond to the main crystallographic axis.

It is generally expected, based on the simulation study and the above arguments, to observe momentum transfers that originate from three different sources, explicit atomic electric fields, polarization-induced electric fields, and deflections arising from breaking symmetry in the scattering geometries as included in the quantity $\vec{\delta}$. The unit cell averaging is supposed to eliminate the atomic electric field contribution. Hence, net deflections either arise from the polarization-induced fields, or from the systematic error $\vec{\delta}$, or a combination of both. Due to screening effects reducing the polarization-induced fields to a large portion, special attention is needed to quantify the local magnitude of $\vec{\delta}$ for the unit cell averaged FM in the following scans. This involves the measurement of the specimen thickness, the mistilt, and requires accompanying simulations to ascertain whether a subsequent interpretation of the measured $\langle \vec{p}_\perp \rangle$ gives rise to potentially present polarization-induced fields.

The FM results are shown in panels (a) of Figures 8 (PZT 1), 9 (PZT 2), and 10 (STO) as a selection of representative data sets in this article, where further data can be found in the Supplementary Material. In PZT 1, three domains can be seen that display slight steps at the domain walls. As expected from the vacuum reference in PZT 2 and STO, the momentum transfer is zero in the vacuum region despite some scan noise. In the two scans, there are no domain boundaries visible. In addition, some slow variations of the FM were observed across all scans.

For the further analysis, bright field (BF) images turned out to be useful. BF images were calculated by integrating the intensity within the Ronchigram as shown in panels (b) of the respective figures. Also in the BF data, domain boundaries are visible as slightly darker regions in the images that exhibit domains, that is, PZT 1. In PZT 2 and STO, the vacuum region can be seen in the upper part of the image. The atomic contrast weakens towards the specimen edge. In the STO scan in Figure 10b, the contrast changes over the whole field of view, indicating thickness and tilt variations.

To separate long-range effects from the atomic contributions, a unit cell averaging procedure was applied to the FM vector field. For this purpose, a unit cell grid was created by a minimum finder to detect atom positions in the virtual BF images. This was refined by applying a center of gravity fit several times until convergence is reached. With the unit cells defined in this way, unit cell averaging led to the data shown color-coded in panels (c) of Figures 8 (PZT 1), 9 (PZT 2), and 10 (STO). The domains can be distinguished clearly from the abrupt changes of the unit cell averaged momentum transfers. Furthermore, the FM changed slowly over the scan area of PZT 1, PZT 2, and STO. Particularly strong changes for the FM at the domain boundary between the upper and middle domain in PZT 1 could be observed.

Without a critical assessment of the systematic error introduced above, these different regimes of the momentum transfer might initially be interpreted as polarization-induced fields. Therefore, a detailed view on tilt and thickness variations is necessary, along with consistency checks of the potential domain structure with the cation displacements in the center of the unit cell, as can be determined from the atomically resolved data.

Although the specimen thickness is too large for a direct interpretation of electrical properties, the divergence of the FM was used (which would otherwise reflect the charge density) to detect the atom positions from the high-resolution 4D-STEM data, as depicted in panels (d) of 8 (PZT 1), 9 (PZT 2), and 10 (STO). Note that in PZT 1 and PZT 2, the oxygen atom columns are clearly visible. In the STO scan, the oxygen columns are only observable in the lower part. The atom positions are needed for unit cell averaging and estimating the polarization direction in order to set up the correct simulations, as detailed below.

The unit cell averaged FMs up to this point did not allow for a consistent conclusion on polarization effects. The FM can be affected significantly by mistilt from a given zone axis. In PZT 1, PZT 2, and STO, Kikuchi bands were present in the diffraction patterns. Because Kikuchi band crossings define the zone axis incidence, Kikuchi band intersections in unit cell averaged diffraction patterns were detected using a procedure which will be reported in more detail elsewhere. With the knowledge of the exact center of the BF disc, the crystallographic mistilt as well as the in-plane rotation can be calculated. The measured 2D tilt maps are shown in Figures 8e, 9e, and 10e. In the case of PZT 1 in Figure 8e, three domains are observable, of which the central one is approximately oriented in zone axis, the upper one shows a mistilt of 2–3 mrad in horizontal direction, and the lower one is tilted by approximately 1–2 mrad vertically. Importantly, the dominant feature is an abrupt change of the crystallographic tilt at the domain boundaries, which are identified to run parallel to the main diagonal. Additionally, the specimen is bent such that the orientation varies at the nanometer scale, even inside the domains. For PZT 2 and STO in Figures 9 and 10, respectively, the tilt maps only show bending. In the STO case, this was expected due to the absence of domains. For PZT 2, either no domain boundary is present in the field of view, or the specimen thickness is too small to allow for a ferroelectric configuration.

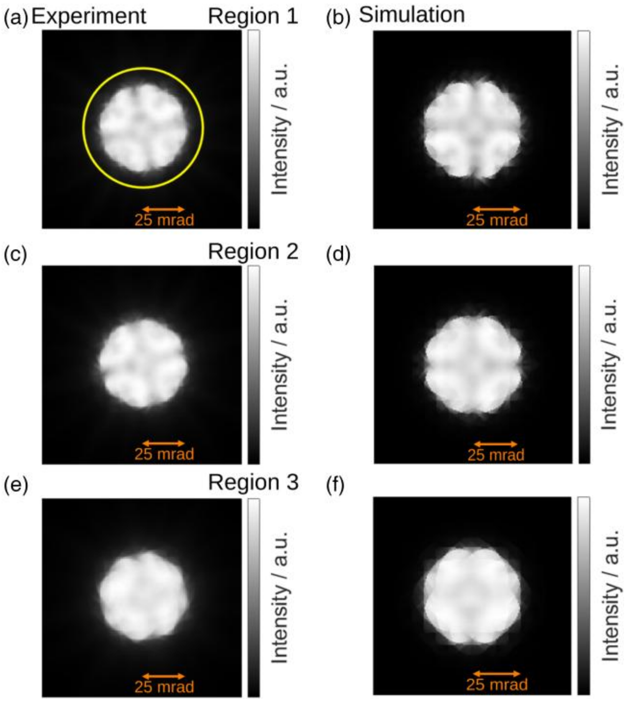

Fig. 11. The PACBEDs of the three regions of PZT 1. *Left:* Experimental data. *Right:* Simulation. The rotation between experiment and simulation is 166°. The virtual CoM-detector is shown as a yellow cycle in (**a**).

Figures 8f, 9f, and 10f show the local in-plane rotation, which concurs with the orientation maps in regard to the domain structure. PZT 1 shows strong domain contrast in a nearly binary map, where the central domain is rotated by 90° in respect to those of the top and bottom. Note that all possible 90° rotations are distinguishable, because inversion symmetry is broken in PZT. No domain contrast can be observed in the rotation maps of the scans of PZT 2 and STO.

In the following, the key observations made in the experiments are reproduced by simulations exemplarily for selected regions. Therefore, evaluation regions were selected that have almost constant parameters such as momentum transfer, crystallographic orientation, in-plane rotation, or thickness. Respective areas are marked in the BF images (Figs. 8b, 9b, and 10b), where all parameters were averaged therein to improve statistics. The displacement of the center atom was also evaluated in the regions. Therefore, the position was calculated relative to the corresponding local unit cell vectors. Afterwards, the symmetry position (0.5, 0.5) was subtracted. Due to the great uncertainties of this type of evaluation in slow STEM scans, the atom displacement was only used as an additional information in order to find the correct domain orientation in comparison with simulations.

The thickness was determined by comparing the PACBED data with a thickness dependent multislice simulation accounting for the estimated mistilt. For PZT 1, this is shown exemplarily in Figure 11. There is a good match between simulation and experiment, except for a slight blurring of the experimental patterns arising from the modulation transfer function (MTF) of the camera, and inelastic scattering due

Table 2. Evaluation Results of Selected Regions from PZT 1.

Region	1	2	3
Experiment			
Orientation	Up	Left	Up
Tilt$_x$ (mrad)	1.6	0.9	−1.0
Tilt$_y$ (mrad)	0.8	−0.4	−0.3
Thickness (nm)	25	20	15
$\Delta E^a_x[\text{reg}_1]$ (MV/cm)	0	−10	40
$\Delta E^a_y[\text{reg}_1]$ (MV/cm)	0	30	10
Simulation			
Displacement$_x$ (u.c.)	0.00	−0.07	0.00
Displacement$_y$ (u.c.)	0.06	0.00	0.06
δ_x (MV/cm)	−40	−10	20
δ_y (MV/cm)	−30	20	10
$\Delta\delta_x[\text{reg}_1]$ (MV/cm)	0	20	60
$\Delta\delta_y[\text{reg}_1]$ (MV/cm)	0	50	40

The displacements are the fit results from the simulated data. The apparent electric fields E^a are given as a difference to region 1 $\Delta E^a[\text{reg}_1]$. δ is also given as a difference relative to region 1 $\Delta\delta[\text{reg}_1]$. All values are given in the coordinate system of the unit cells and are rounded to significant digits.

to plasmon excitations (Beyer et al., 2020; Robert et al., 2022).

The results are shown in Tables 2 and 3 and the Supplementary Material. Note the tilt and thickness variations within the same scan, and that an apparent electric field was found in STO that additionally varies across the scan region. Importantly, the apparent field is denoted by superscript E^a. It describes the electric field obtained from the momentum transfer. If the origin of momentum space was obtained from vacuum regions as described above, it is denoted as $\Delta E^a_{x/y}[\text{vac}]$. As we have previously elaborated some difficulties in using this procedure, we additionally provide the field differences with respect to one of the regions as denoted with $\Delta E^a_{x/y}[\text{reg}_n]$ with n as the region number.

The field components $\Delta E^a_{x/y}[\text{vac}]$ in Table 3 adopt relatively large values of hundreds of MV/cm in STO which are significantly higher than the simulated systematic errors arising from mistilts in Figure 6 due to the ambiguous choice of the origin in momentum space. However, treating this ambiguity as approximately constant, i.e., an offset to all measurements, the relative differences expressed by $\Delta E^a_{x/y}[\text{reg}_1]$ in Table 3 correspond well with the simulated range of systematic errors. In particular, the simulation taking the experimentally measured geometries into account explicitly are also shown in Table 3. Systematic errors $\Delta\delta_{x/y}[\text{reg}_1]$ take values of some ten MV/cm, similar to $\Delta E^a_{x/y}[\text{reg}_1]$ determined experimentally. It is apparent that the simulated systematic errors δ reflect the correct order of magnitude as to $\Delta E^a_{x/y}[\text{reg}_1]$, but sometimes deviate numerically from the experiment. This is understandable due to the partly strong gradients of δ with respect to mistilt and specimen thickness, as implied by Figure 6. In general, curved specimen surfaces and thickness gradients have not been included explicitly in the simulations for Tables 2 and 3, meaning that the thickness and orientation dependence always assumed parallel-sided slabs of a bulk crystal.

Table 3. Evaluation Results of Selected Regions from STO.

Region	1	2	3	4	5
Experiment					
Tilt$_x$ (mrad)	1.7	1.7	1.6	1.7	0.8
Tilt$_y$ (mrad)	1.3	1.0	0.5	−0.5	−1.2
Thickness (nm)	30	25	20	15	10
$\Delta E^a_x[\text{vac}]$ (MV/cm)	30	30	30	30	50
$\Delta E^a_y[\text{vac}]$ (MV/cm)	−220	−200	−220	−190	−220
$\Delta E^a_x[\text{reg}_1]$ (MV/cm)	0	0	10	10	30
$\Delta E^a_y[\text{reg}_1]$ (MV/cm)	0	20	10	30	10
Simulation					
Displacement$_x$ (u.c.)	0.00	0.00	0.00	0.00	0.00
Displacement$_y$ (u.c.)	0.00	0.00	0.00	0.00	0.00
δ_x (MV/cm)	−20	−30	−40	−30	−10
δ_y (MV/cm)	−20	−20	−10	10	20
$\Delta\delta_x[\text{reg}_1]$ (MV/cm)	0	−10	−20	0	10
$\Delta\delta_y[\text{reg}_1]$ (MV/cm)	0	0	10	30	40

The displacements are the fit results from the simulated data. The apparent electric fields E^a are given as a difference to vacuum $\Delta E^a[\text{vac}]$ and to region 1 $\Delta E^a[\text{reg}_1]$. δ is also given as a difference relative to region 1 $\Delta\delta[\text{reg}_1]$. All values are given in the coordinate system of the unit cells and are rounded to significant digits.

To conclude the accompanying simulations, they led to systematic errors well reflecting the orders of magnitude of the apparently measured electric fields in all cases. Moreover, the experimentally determined thicknesses and mistilts using state-of-the-art methodologies are not precise enough to numerically provide exactly the same magnitudes for $\Delta\delta$ and ΔE^a, and including fully realistic specimen geometries with surface normal and thickness gradients would be necessary. However, including these effects is not advisable here since the experimental data at hand did not allow measuring the respective quantities which would be needed as input for the simulations. Consequently, no evidence of the presence of polarization-induced electric fields were found in the specimens investigated, despite the strong domain contrast of the FM signal averaged over unit cells.

Discussion

Simulation Study

Equation (10) shows that quantifying the systematic error for the experimental setup and material system is important for quantitative measurements of mesoscopic electric fields by means of unit cell averaged FM data. The simulations with different atom displacements in Figure 2 show that the origin of the systematic error is a dynamical scattering effect that does not cancel in unit cell averages due to broken symmetry. This effect already plays a role for very thin specimens. The behavior of the systematic error at different acceleration voltages in Figure 3 is explainable because the interaction constant is smaller for higher energies, i.e., higher acceleration voltage. Thus, it is advisable to use an acceleration voltage as high as possible in the limit of the microscope capability or potential radiation damage of the sample. The behavior of the systematic error for different convergence angles (Fig. 4) advises to use rather large convergence angles within the limit set by the probe aberration corrector.

For thick specimens ($\gtrsim$30 nm), bonding effects (Fig. 5) can make a further contribution to the systematic error and should be taken into account to quantify the systematic error $\vec{\delta}$. Between 10 and 30 nm, neglect of bonding can result in errors of up to 25% of the true value; nevertheless, the contribution of bonding is much lower as compared to the ionic displacements or mistilt. The tilted simulations in Figure 6 show that even in a nonferroelectric material the formally calculated unit cell averaged electric field appears to be nonzero, meaning that tilt effects need to be addressed in detail in ferroelectrics, because tilt gradients could easily be misinterpreted as internal electric fields. In general, the sample should be oriented perfectly in zone axis if possible.

However, our experimental study showed that domain boundaries in PZT are inherently connected with an abrupt change of specimen tilt.

Application Aspects

The evaluation of the BF-STEM showed contrast variations in PZT 2 and STO, which could be explained by thickness variations of the sample. In STO, this variation changes slowly over the whole scan, as is supported by the thickness measurement in Table 3. In PZT, thickness also changes quite abruptly across domain boundaries. A detailed discussion of various interface effects that could cause the slightly darker BF contrast at the domain boundaries in some cases is out of the scope of this paper. Qualitatively, domain boundaries constitute interfaces with strain, rotation, and static disorder which is usually a source of Huang scattering to rather high angles constituting an additional scattering channel that can decrease the BF signal.

The evaluation of the unit cell averaged FM indicates that this method provides significant domain contrast. In PZT 2, it seems that there are no domains near the surface. This could be verified by the rotation analysis. The slow variations of the FM in all scans can be assigned to specimen bending. Qualitatively this can explain the behavior of the corresponding unit cell averaged FM results. It is expected that there is no quantitative match as the FM is also sensitive to sample thickness where the tilt map is not. The PZT 1 data show an additional effect as depicted in Figure 7, where FM gradients arise from a different tilt of the domains. The tilt analysis of PZT 1 supports this. The kinks originate from mismatches at the domain boundaries as an effect that can easily occur in ferroelectric-ferroelastic materials (Catalan et al., 2011). Under these conditions, it is impossible to bring more than one domain in zone axis in the same scan. This will result in different systematic errors on the apparent electric field in different domains. The FMs at the domain boundary between the upper and the central domain have a rather large magnitude, most probably due to interface effects (Grieb et al., 2021) caused by probe broadening in thick samples and the simultaneous interaction with two different regions.

The rotation analysis of PZT 1 gives a strong domain contrast. The disadvantage is that only a relative rotation can be gained and no information about the magnitude of the polarization is provided. Finding the actual domain orientation in at least one domain requires additional evaluations.

In STO, the electric field has a large constant mismatch giving a strong hint that using a vacuum region in the same scan is not a reliable method to define the reference point of zero momentum transfer. In PZT 1, the domain configuration is consistent with Denneulin et al. (2018), i.e., c-a-c domains. Overall, measuring the electric fields potentially present in ferroelectrics remains a challenging task, as this work already demonstrates the complexity of signal formation in real specimen when electric fields are not taken into account.

Structural Characterization

The polarization can, in principle, also be determined using structural information, especially via evaluating the atom positions inside a unit cell. The atom positions can be fitted from negative C_s imaging (Jia et al., 2003, 2008), low angle annular dark field STEM, annular BF STEM, integrated DPC STEM, and imaging STEM. A comparison of these methods was presented by Gauquelin et al. (2017). However, atom position measurement methods only yield accurate values if the specimen is in zone axis (Zhou et al., 2016). This is problematic in cases dealt with in the present study, where imaging multiple domains at once in zone axis is inhibited by abrupt tilt changes at domain boundaries.

Conclusion

To characterize ferroelectric materials by unit cell averaged FM data, a variety of sources of systematic errors needs to be taken into account. In particular, these are atom displacements from the symmetry positions, the magnitude of the acceleration voltage, STEM probe semi-convergence angle, sample thickness and sample tilt out of zone axis. Simulations showed that a systematic error of the calculated electric fields using the unit cell averaged momentum transfer originates from the violation of point symmetry within the unit cells, and takes values that can easily exceed potential polarization-induced electric fields in ferroelectrics.

Importantly, the systematic error produces deflection gradients between different domains which are apparently representative of measured fields. However, it could be shown that for PZT at least, many adjacent domains exhibit a relative crystallographic mistilt and in-plane rotation. A direct interpretation of ferroelectric polarization therefore needs to be carefully conducted. The experimental result of Strontium Titanate showed that even defining the zero point of the momentum transfer is rather ambiguous under real conditions, which makes absolute values of the simulated electric fields less reliable. The experimental results from PZT showed that the method gives qualitative domain contrast. In order to obtain the correct domain configurations, there needs to be systematic comparison with simulations of all possible domain configurations. Comparison of the relative calculated electric field with the relative systematic error revealed that the domain contrast of the unit cell averaged electric fields was, at least in the present PZT specimens, mainly caused by dynamical scattering effects and the electric field plays only a minor role, if present at all.

Supplementary Material

To view supplementary material for this article, please visit https://doi.org/10.1093/micmic/ozad016.

Acknowledgments

Support from Thermo Fisher Scientific via providing the EMPAD detector to acquire momentum-resolved STEM data is gratefully acknowledged.

Financial Support

K.M.-C. and B.M. acknowledge funding from the Deutsche Forschungsgemeinschaft under grant number EXC 2089/1-390776260 (Germany's Excellence Strategy). K.M.-C. and A.S. were supported by the Helmholtz Association (Germany) under contracts VH-NG-1317 and ZT-I-0025. A.R. was supported by the DFG under contract RO2057/14.

Conflict of Interest

The authors do not declare additional ones than the given affiliations and fundings.

References

Ballabriga R, Campbell M, Heijne E, Llopart X, Tlustos L & Wong W (2011). Medipix3: A 64k pixel detector readout chip working in single photon counting mode with improved spectrometric performance. *Nucl Instrum Methods Phys Res A* **633**, S15–S18. https://doi.org/10.1016/j.nima.2010.06.108

Bauer B, Hubmann J, Lohr M, Reiger E, Bougeard D & Zweck J (2014). Direct detection of spontaneous polarization in wurtzite GaAs nanowires. *Appl Phys Lett* **104**, 211902. https://doi.org/10.1063/1.4880209

Beklešovas B, Iljinas A, Stankus V, Čyvienė J, Andrulevičius M, Ivanov M & Banys J (2022). Structural, morphologic, and ferroelectric properties of PZT films deposited through layer-by-layer reactive DC magnetron sputtering. *Coatings* **12**, 717. https://doi.org/10.3390/coatings12060717

Bethe H (1930). Zur theorie des durchgangs schneller korpuskularstrahlen durch materie. *Ann Phys* **397**, 325–400. https://doi.org/10.1002/(ISSN)1521-3889

Beyer A, Krause FF, Robert HL, Firoozabadi S, Grieb T, Kükelhahn P, Heimes D, Schowalter M, Müller-Caspary K, Rosenauer A & Volz K (2020). Influence of plasmon excitations on atomic-resolution quantitative 4d scanning transmission electron microscopy. *Sci Rep* **10**, 17890. https://doi.org/10.1038/s41598-020-74434-w

Beyer A, Munde MS, Firoozabadi S, Heimes D, Grieb T, Rosenauer A, Müller-Caspary K & Volz K (2021). Quantitative characterization of nanometer-scale electric fields via momentum-resolved STEM. *Nano Lett* **21**, 2018–2025. https://doi.org/10.1021/acs.nanolett.0c04544

Blaha P, Schwarz K, Tran F, Laskowski R, Madsen GKH & Marks LD (2020). WIEN2k: An APW+lo program for calculating the properties of solids. *J Chem Phys* **152**, 074101. https://doi.org/10.1063/1.5143061

Campanini M, Eimre K, Bon M, Pignedoli CA, Rossell MD & Erni R (2020). Atomic-resolution differential phase contrast STEM on ferroelectric materials: A mean-field approach. *Phys Rev B* **101**, 184116. https://doi.org/10.1103/PhysRevB.101.184116

Carlier T, Chambrier MH, Costa AD, Blanchard F, Denneulin T, Létiche M, Roussel P, Desfeux R & Ferri A (2020). Ferroelectric state in an α-nd2wo6 polymorph stabilized in a thin film. *Chem Mater* **32**, 7188–7200. https://doi.org/10.1021/acs.chemmater.0c01405

Catalan G, Lubk A, Vlooswijk AHG, Snoeck E, Magen C, Janssens A, Rispens G, Rijnders G, Blank DHA & Noheda B (2011). Flexoelectric rotation of polarization in ferroelectric thin films. *Nat Mater* **10**, 963–967. https://doi.org/10.1038/nmat3141

Chang HJ, Kalinin SV, Morozovska AN, Huijben M, Chu YH, Yu P, Ramesh R, Eliseev EA, Svechnikov GS, Pennycook SJ & Borisevich AY (2011). Atomically resolved mapping of polarization and electric fields across ferroelectric/oxide interfaces by z-contrast imaging. *Adv Mater* **23**, 2474–2479. https://doi.org/10.1002/adma.201004641

Chen A, Lv Y, Su L & Zhu Y (2022). Sub-band response of PZT photodetector controlled by back-gate voltage. *J Phys D: Appl Phys* **55**, 505104. https://doi.org/10.1088/1361-6463/ac9d47

Close R, Chen Z, Shibata N & Findlay S (2015). Towards quantitative, atomic-resolution reconstruction of the electrostatic potential via differential phase contrast using electrons. *Ultramicroscopy* **159**, 124–137. https://doi.org/10.1016/j.ultramic.2015.09.002

Copie O, Chevalier N, Rhun GL, Rountree CL, Martinotti D, Gonzalez S, Mathieu C, Renault O & Barrett N (2017). Adsorbate screening of surface charge of microscopic ferroelectric domains in sol–gel PbZr0.2ti0.8o3 thin films. *ACS Appl Mater Interfaces* **9**, 29311–29317. https://doi.org/10.1021/acsami.7b08925

Cowley JM & Moodie AF (1957). The scattering of electrons by atoms and crystals. I. A new theoretical approach. *Acta Crystallogr* **10**, 609–619. https://doi.org/10.1107/S0365110X57002194

Cowley JM & Moodie AF (1959). The scattering of electrons by atoms and crystals. III. Single-crystal diffraction patterns. *Acta Crystallogr* **12**, 360–367. https://doi.org/10.1107/S0365110X59001104

Dawber M, Rabe KM & Scott JF (2005). Physics of thin-film ferroelectric oxides. *Rev Mod Phys* **77**, 1083–1130. https://doi.org/10.1103/RevModPhys.77.1083

Deguchi M, Tanaka S & Tanji T (2010). Determination of piezoelectric fields across InGaN/GaN quantum wells by means of electron holography. *J Electron Mater* **39**, 815–818. https://doi.org/10.1007/s11664-010-1092-9

Denneulin T & Everhardt AS (2022). A transmission electron microscopy study of low-strain epitaxial BaTiO$_3$ grown onto NdScO$_3$. *J Phys: Condens Matter* **34**, 235701. https://doi.org/10.1088/1361-648X/ac5db3

Denneulin T, Wollschläger N, Everhardt AS, Farokhipoor S, Noheda B, Snoeck E & Hÿtch M (2018). Local deformation gradients in epitaxial Pb(Zr$_{0.2}$Ti$_{0.8}$)O$_3$ layers investigated by transmission electron microscopy. *J Phys: Condens Matter* **30**, 215701. https://doi.org/10.1088/1361-648X/aabd00

Ding J, Shao DF, Li M, Wen LW & Tsymbal EY (2021). Two-dimensional antiferroelectric tunnel junction. *Phys Rev Lett* **126**, 057601. https://doi.org/10.1103/PhysRevLett.126.057601

Ehrenfest P (1927). Bemerkung über die angenäherte gültigkeit der klassischen mechanik innerhalb der quantenmechanik. *Z Phys* **45**, 455–457. https://doi.org/10.1007/BF01329203

Everhardt AS, Denneulin T, Grünebohm A, Shao YT, Ondrejkovic P, Zhou S, Domingo N, Catalan G, Hlinka J, Zuo JM, Matzen S & Noheda B (2020). Temperature-independent giant dielectric response in transitional BaTiO$_3$ thin films. *Appl Phys Rev* **7**, 011402. https://doi.org/10.1063/1.5122954

Ferrero G, Astafiev K, Ringgaard E, de Oliveira LS, Sudireddy BR, Haugen AB, Žiberna K, Malič B & Rojac T (2023). Piezoelectric properties of mechanochemically processed 0.67BiFeO$_3$–0.33BaTiO$_3$ ceramics. *J Eur Ceram Soc* **43**, 350–361. https://doi.org/10.1016/j.jeurceramsoc.2022.10.024

Frabboni S, Matteucci G & Pozzi G (1987). Observation of electrostatic fields by electron holography: The case of reverse-biased p-n junctions. *Ultramicroscopy* **23**, 29–37. https://doi.org/10.1016/0304-3991(87)90224-5

Frantti J, Lappalainen J, Eriksson S, Lantto V, Nishio S, Kakihana M, Ivanov S & Rundlöf H (2000). Neutron diffraction studies of Pb(Zr$_x$Ti$_{1-x}$)O$_3$ ceramics. *Jpn J Appl Phys* **39**, 5697–5703. https://doi.org/10.1143/JJAP.39.5697

Gao W, Addiego C, Wang H, Yan X, Hou Y, Ji D, Heikes C, Zhang Y, Li L, Huyan H, Blum T, Aoki T, Nie Y, Schlom DG, Wu R & Pan X (2019). Real-space charge-density imaging with sub-ångström resolution by four-dimensional electron microscopy. *Nature* **575**, 480–484. https://doi.org/10.1038/s41586-019-1649-6

Gao P, Zhang Z, Li M, Ishikawa R, Feng B, Liu HJ, Huang YL, Shibata N, Ma X, Chen S, Zhang J, Liu K, Wang EG, Yu D, Liao L, Chu YH & Ikuhara Y (2017). Possible absence of critical thickness and size effect in ultrathin perovskite ferroelectric films. *Nat Commun* **8**, 15549. https://doi.org/10.1038/ncomms15549

Garcia V & Bibes M (2014). Ferroelectric tunnel junctions for information storage and processing. *Nat Commun* **5**, 4289. https://doi.org/10.1038/ncomms5289

Gauquelin N, Béché A, Krause F, Lobato I, Lazar S, Rosenauer A, Van Aert S & Verbeeck J (2017). Determining oxygen relaxations at an interface: A comparative study between transmission electron microscopy techniques. *Ultramicroscopy* **181**, 178–190. https://doi.org/10.1016/j.ultramic.2017.06.002

Grieb T, Krause FF, Müller-Caspary K, Ritz R, Simson M, Schörmann J, Mahr C, Müssener J, Schowalter M, Soltau H, Eickhoff M & Rosenauer A (2021). 4D-STEM at interfaces to GaN: Center-of-mass approach & NBED-disc detection. *Ultramicroscopy* **228**, 113321. https://doi.org/10.1016/j.ultramic.2021.113321

Gruverman A, Alexe M & Meier D (2019). Piezoresponse force microscopy and nanoferroic phenomena. *Nat Commun* **10**, 1661. https://doi.org/10.1038/s41467-019-09650-8

Gruverman A & Kalinin SV (2006). Piezoresponse force microscopy and recent advances in nanoscale studies of ferroelectrics. *J Mater Sci* **41**, 107–116. https://doi.org/10.1007/s10853-005-5946-0

Haas B, Rouvière JL, Boureau V, Berthier R & Cooper D (2019). Direct comparison of off-axis holography and differential phase contrast for the mapping of electric fields in semiconductors by transmission electron microscopy. *Ultramicroscopy* **198**, 58–72. https://doi.org/10.1016/j.ultramic.2018.12.003

Heggen M, Luysberg M & Tillmann K (2016). FEI titan 80-300 STEM. *J Large-Scale Res Facilities* **2**, A42. https://doi.org/10.17815/jlsrf-2-67

Jia CL, Lentzen M & Urban K (2003). Atomic-resolution imaging of oxygen in perovskite ceramics. *Science* **299**, 870–873. https://doi.org/10.1126/science.1079121

Jia CL, Mi SB, Urban K, Vrejoiu I, Alexe M & Hesse D (2007). Atomic-scale study of electric dipoles near charged and uncharged domain walls in ferroelectric films. *Nat Mater* **7**, 57–61. https://doi.org/10.1038/nmat2080

Jia CL, Mi SB, Urban K, Vrejoiu I, Alexe M & Hesse D (2008). Atomic-scale study of electric dipoles near charged and uncharged domain walls in ferroelectric films. *Nat Mater* **7**, 57–61. https://doi.org/10.1038/nmat2080

Jia CL, Nagarajan V, He JQ, Houben L, Zhao T, Ramesh R, Urban K & Waser R (2006). Unit-cell scale mapping of ferroelectricity and tetragonality in epitaxial ultrathin ferroelectric films. *Nat Mater* **6**, 64–69. https://doi.org/10.1038/nmat1808

Kalinin SV, Kim Y, Fong DD & Morozovska AN (2018). Surface-screening mechanisms in ferroelectric thin films and their effect on polarization dynamics and domain structures. *Rep Prog Phys* **81**, 036502. https://doi.org/10.1088/1361-6633/aa915a

Karthik J, Damodaran AR & Martin LW (2012). Effect of 90° domain walls on the low-field permittivity of $PbZr_{0.2}Ti_{0.8}O_3$ thin films. *Phys Rev Lett* **108**, 167601. https://doi.org/10.1103/PhysRevLett.108.167601

Kwei GH, Lawson AC, Billinge SJL & Cheong SW (1993). Structures of the ferroelectric phases of barium titanate. *J Phys Chem* **97**, 2368–2377. https://doi.org/10.1021/j100112a043

Kwon O, Seol D, Qiao H & Kim Y (2020). Recent progress in the nanoscale evaluation of piezoelectric and ferroelectric properties via scanning probe microscopy. *Adv Sci* **7**, 1901391. https://doi.org/10.1002/advs.201901391

Lazić I & Bosch E (2017). Phase contrast stem for thin samples: Integrated differential phase contrast. *Adv Imaging Electron Phys* **199**, 75. https://doi.org/10.1016/bs.aiep.2017.01.006

Lazić I, Bosch EG & Lazar S (2016). Phase contrast STEM for thin samples: Integrated differential phase contrast. *Ultramicroscopy* **160**, 265–280. https://doi.org/10.1016/j.ultramic.2015.10.011

Leal SH, Sczancoski JC, Cavalcante LS, Escote MT, Matos JME, Santos MRMC, Pontes FM, Longo E & Varela JA (2009). Structural and morphological characteristics of $(Pb_{1-x}Sr_x)TiO_3$ powders obtained by polymeric precursor method. *J Sol–Gel Sci Technol* **53**, 21–29. https://doi.org/10.1007/s10971-009-2049-4

Lichte H (1986). Electron holography approaching atomic resolution. *Ultramicroscopy* **20**, 293–304. https://doi.org/10.1016/0304-3991(86)90193-2

Lichte H (1991). Optimum focus for taking electron holograms. *Ultramicroscopy* **38**, 13–22. https://doi.org/10.1016/0304-3991(91)90105-F

Lichte H (1993). Parameters for high-resolution electron holography. *Ultramicroscopy* **51**, 15–20. https://doi.org/10.1016/0304-3991(93)90131-G

Lichte H (2008). Performance limits of electron holography. *Ultramicroscopy* **108**, 256–262. https://doi.org/10.1016/j.ultramic.2007.06.006

Lichte H, Geiger D, Harscher A, Heindl E, Lehmann M, Malamidis D, Orchowski A & Rau WD (1996). Artefacts in electron holography. *Ultramicroscopy* **64**, 67–77. https://doi.org/10.1016/0304-3991(96)00018-6

Lichte H & Lehmann M (2008). Electron holography-basics and applications. *Rep Prog Phys* **71**, 016102. https://doi.org/10.1088/0034-4885/71/1/016102

Lichte H, Reibold M, Brand K & Lehmann M (2002). Ferroelectric electron holography. *Ultramicroscopy* **93**, 199–212. https://doi.org/10.1016/S0304-3991(02)00277-2

Lobato I & Dyck DV (2014). An accurate parameterization for scattering factors, electron densities and electrostatic potentials for neutral atoms that obey all physical constraints. *Acta Crystallogr Sect A Found Adv* **70**, 636–649. https://doi.org/10.1107/S205327331401643X

Lohr M, Schregle R, Jetter M, Wächter C, Müller-Caspary K, Mehrtens T, Rosenauer A, Pietzonka I, Strassburg M & Zweck J (2015). Quantitative measurements of internal electric fields with differential phase contrast microscopy on InGaN/GaN quantum well structures. *Phys Stat Sol (b)* **253**, 140–144. https://doi.org/10.1002/pssb.201552288

Lohr M, Schregle R, Jetter M, Wächter C, Wunderer T, Scholz F & Zweck J (2012). Differential phase contrast 2.0—Opening new "fields" for an established technique. *Ultramicroscopy* **117**, 7–14. https://doi.org/10.1016/j.ultramic.2012.03.020

Lubk A & Zweck J (2015). Differential phase contrast: An integral perspective. *Phys Rev A* **91**, 023805. https://doi.org/10.1103/PhysRevA.91.023805

Ma Y, Song J, Wang X, Liu Y & Zhou J (2021). Synthesis, microstructure and properties of magnetron sputtered lead zirconate titanate (PZT) thin film coatings. *Coatings* **11**, 944. https://doi.org/10.3390/coatings11080944

MacLaren I, Wang L, McGrouther D, Craven AJ, McVitie S, Schierholz R, Kovács A, Barthel J & Dunin-Borkowski RE (2015). On the origin of differential phase contrast at a locally charged and globally charge-compensated domain boundary in a polar-ordered material. *Ultramicroscopy* **154**, 57–63. https://doi.org/10.1016/j.ultramic.2015.03.016

McCartney MR, Dunin-Borkowski RE & Smith DJ (2019). Quantitative measurement of nanoscale electrostatic potentials and charges using off-axis electron holography: Developments and opportunities. *Ultramicroscopy* **203**, 105–118. https://doi.org/10.1016/j.ultramic.2019.01.008

McCartney MR, Smith DJ, Hull R, Bean JC, Voelkl E & Frost B (1994). Direct observation of potential distribution across Si/Si p-n junctions using off-axis electron holography. *Appl Phys Lett* **65**, 2603–2605. https://doi.org/10.1063/1.112581

Meng K, Li W, Tang XG, Liu QX & Jiang YP (2022). A review of a good binary ferroelectric ceramic: $BaTiO_3$–$BiFeO_3$. *ACS Appl Electron Mater* **4**, 2109–2145. https://doi.org/10.1021/acsaelm.1c00109

Mott NF (1930). The scattering of electrons by atoms. *Proc R Soc Lond A* **127**, 658–665. https://doi.org/10.1098/rspa.1930.0082

Müller-Caspary K, Duchamp M, Rösner M, Migunov V, Winkler F, Yang H, Huth M, Ritz R, Simson M, Ihle S, Soltau H, Wehling T, Dunin-Borkowski RE, Van Aert S & Rosenauer A (2018). Atomic-scale quantification of charge densities in two-dimensional materials. *Phys Rev B* **98**, 121408. https://doi.org/10.1103/PhysRevB.98.121408

Müller-Caspary K, Grieb T, Müßener J, Gauquelin N, Hille P, Schörmann J, Verbeeck J, Van Aert S, Eickhoff M & Rosenauer A (2019*a*). Electrical polarization in AlN/GaN nanodisks measured by momentum-resolved 4D scanning transmission electron microscopy. *Phys Rev Lett* **122**, 106102. https://doi.org/10.1103/PhysRevLett.122.106102

Müller-Caspary K, Krause FF, Grieb T, Löffler S, Schowalter M, Béché A, Galioit V, Marquardt D, Zweck J, Schattschneider P, Verbeeck J & Rosenauer A (2017). Measurement of atomic electric fields and charge densities from average momentum transfers using scanning transmission electron microscopy. *Ultramicroscopy* **178**, 62–80. https://doi.org/10.1016/j.ultramic.2016.05.004

Müller-Caspary K, Krause FF, Winkler F, Béché A, Verbeeck J, Aert SV & Rosenauer A (2019*b*). Comparison of first moment STEM with conventional differential phase contrast and the dependence on electron dose. *Ultramicroscopy* **203**, 95–104. https://doi.org/10.1016/j.ultramic.2018.12.018

Müller-Caspary K, Oelsner A & Potapov P (2015). Two-dimensional strain mapping in semiconductors by nano-beam electron diffraction employing a delay-line detector. *Appl Phys Lett* **107**, 072110. https://doi.org/10.1063/1.4927837

Müller K, Krause FF, Béché A, Schowalter M, Galioit V, Löfler S, Verbeeck J, Zweck J, Schattschneider P & Rosenauer A (2014). Atomic electric fields revealed by a quantum mechanical approach to electron picodiffraction. *Nat Commun* **5**, 5653. https://doi.org/10.1038/ncomms6653

Müller K, Rosenauer A, Schowalter M, Zweck J, Fritz R & Volz K (2012). Strain measurement in semiconductor heterostructures by scanning transmission electron microscopy. *Microsc Microanal* **18**, 995–1009. https://doi.org/10.1017/S1431927612001274

Müller K, Ryll H, Ordavo I, Schowalter M, Zweck J, Soltau H, Ihle S, Strüder L, Volz K, Potapov P & Rosenauer A (2013). STEM strain analysis at sub-nanometre scale using millisecond frames from a direct electron read-out CCD camera. *J Phys Conf Ser* **471**, 012024. https://doi.org/10.1088/1742-6596/471/1/012024

Müller K, Schowalter M, Rosenauer A, Rubel O & Volz K (2010). Effect of bonding and static atomic displacements on composition quantification in $In_xGa_{1-x}N_yAs_{1-y}$. *Phys Rev B* **81**, 075315. https://doi.org/10.1103/PhysRevB.81.075315

Parker DS, Herklotz A, Ward TZ, McGuire MA & Singh DJ (2016). Enhanced ferroelectric polarization and possible morphotrophic phase boundary in PZT-based alloys. *Phys Rev B* **93**, 174307. https://doi.org/10.1103/PhysRevB.93.174307

Pintilie L, Boni GA, Chirila C, Hrib L, Trupina L, Filip LD & Pintilie I (2020). Polarization switching and negative capacitance in epitaxial $PbZr_{0.2}Ti_{0.8}O_3$ thin films. *Phys Rev Appl* **14**, 014080. https://doi.org/10.1103/PhysRevApplied.14.014080

Plackett R, Horswell I, Gimenez EN, Marchal J, Omar D & Tartoni N (2013). Merlin: A fast versatile readout system for Medipix3. *J Instrum* **8**, C01038–C01038. https://doi.org/10.1088/1748-0221/8/01/C01038

Robert HL, Diederichs B & Müller-Caspary K (2022). Contribution of multiple plasmon scattering in low-angle electron diffraction investigated by energy-filtered atomically resolved 4D-STEM. *Appl Phys Lett* **121**, 213502. https://doi.org/10.1063/5.0129692

Rosenauer A & Schowalter M (2008). STEMSIM—A new software tool for simulation of STEM HAADF Z-contrast imaging. In *Microscopy of Semiconducting Materials*, Cullis A G & Midgley P A (Eds.), vol. **120**. pp. 169–172. Dordrecht: Springer.

Rosenauer A, Schowalter M, Glas F & Lamoen D (2005). First-principles calculations of 002 structure factors for electron scattering in strained $In_xGa_{1-x}As$. *Phys Rev B* **72**, 085326. https://doi.org/10.1103/PhysRevB.72.085326

Ryll H, Simson M, Hartmann R, Holl P, Huth M, Ihle S, Kondo Y, Kotula P, Liebel A, Müller-Caspary K, Rosenauer A, Sagawa R, Schmidt J, Soltau H & Strüder L (2016). A pnCCD-based, fast direct single electron imaging camera for TEM and STEM. *J Instrum* **11**, P04006–P04006. https://doi.org/10.1088/1748-0221/11/04/P04006

Shibata N, Findlay SD, Kohno Y, Sawada H, Kondo Y & Ikuhara Y (2012). Differential phase-contrast microscopy at atomic resolution. *Nat Phys* **8**, 611–615. https://doi.org/10.1038/nphys2337

Shibata N, Findlay SD, Sasaki H, Matsumoto T, Sawada H, Kohno Y, Otomo S, Minato R & Ikuhara Y (2015). Imaging of built-in electric field at a p-n junction by scanning transmission electron microscopy. *Sci Rep* **5**, 10040. https://doi.org/10.1038/srep10040

Shibata N, Seki T, Sánchez-Santolino G, Findlay SD, Kohno Y, Matsumoto T, Ishikawa R & Ikuhara Y (2017). Electric field imaging of single atoms. *Nat Commun* **8**, 15631. https://doi.org/10.1038/ncomms15631

Shin C (2019). Experimental understanding of polarization switching in PZT ferroelectric capacitor. *Semicond Sci Technol* **34**, 075004. https://doi.org/10.1088/1361-6641/ab1d2e

Tao LL & Tsymbal EY (2021). Perspectives of spin-textured ferroelectrics. *J Phys D: Appl Phys* **54**, 113001. https://doi.org/10.1088/1361-6463/abcc25

Tate MW, Purohit P, Chamberlain D, Nguyen KX, Hovden R, Chang CS, Deb P, Turgut E, Heron JT, Schlom DG, Ralph DC, Fuchs GD, Shanks KS, Philipp HT, Muller DA & Gruner SM (2016). High dynamic range pixel array detector for scanning transmission electron microscopy. *Microsc Microanal* **22**, 237–249. https://doi.org/10.1017/S1431927615015664

Vandana Gupta, Tandon RP & Gupta V (2021). Impact of TiO_2 buffer layer on the ferroelectric photovoltaic response of CSD grown PZT thick films. *Appl Phys A* **127**, 427. https://doi.org/10.1007/s00339-021-04552-3

van der Veer E, Noheda B & Acuautla M (2021). Piezoelectric properties of PZT by an ethylene glycol-based chemical solution synthesis. *J Solgel Sci Technol* **100**, 517–525. https://doi.org/10.1007/s10971-021-05651-6

Voelkl E, Zheng F, Migunov V, Beleggia M & Dunin-Borkowski R (2019). Live measurement of electrical charge density in materials using off-axis electron holography. *Microsc Microanal* **25**, 44–45. https://doi.org/10.1017/S1431927619000953

Vrejoiu I, Rhun GL, Zakharov ND, Hesse D, Pintilie L & Alexe M (2006). Threading dislocations in epitaxial ferroelectric $PbZr_{0.2}Ti_{0.8}O_3$ films and their effect on polarization backswitching. *Philos Mag* **86**, 4477–4486. https://doi.org/10.1080/14786430600728653

Waddell E & Chapman J (1979). Linear imaging of strong phase objects using asymmetrical detectors in STEM. *Optic* **54**, 83–96.

Wei L, Li C, Guan L & Guo J (2021). Enhancing ferroelectric photovoltaic effect of $BaTiO_3$ by the lateral interface. *Surf Interface Anal* **53**, 773–778. https://doi.org/10.1002/sia.6978

Wen Z, Li C, Wu D, Li A & Ming N (2013). Ferroelectric-field-effect-enhanced electroresistance in metal/ferroelectric/semiconductor tunnel junctions. *Nat Mater* **12**, 617–621. https://doi.org/10.1038/nmat3649

Xu Q & Li Z (2020). Dielectric and ferroelectric behaviour of Zr-doped $BaTiO_3$ perovskites. *Process Appl Ceram* **14**, 188–194. https://doi.org/10.2298/PAC2003188X

Yazdi S, Kasama T, Beleggia M, Yekta MS, McComb DW, Twitchett-Harrison AC & Dunin-Borkowski RE (2015). Towards quantitative electrostatic potential mapping of working semiconductor devices using off-axis electron holography. *Ultramicroscopy* **152**, 10–20. https://doi.org/10.1016/j.ultramic.2014.12.012

Yücelen E, Lazić I & Bosch EGT (2018). Phase contrast scanning transmission electron microscopy imaging of light and heavy atoms at the limit of contrast and resolution. *Sci Rep* **8**, 2676. https://doi.org/10.1038/s41598-018-20377-2

Zhang Y, Yang Q, Tao L, Tsymbal EY & Alexandrov V (2020). Effects of strain and film thickness on the stability of the rhombohedral phase of HfO_2. *Phys Rev Appl* **14**, 014068. https://doi.org/10.1103/PhysRevApplied.14.014068

Zhao YP, Wang C, Zheng XF, Ma XH, Li A, Liu K, He YL, Lu XL & Hao Y (2021). Ferroelectric effect and equivalent polarization charge model of $PbZr_{0.2}Ti_{0.8}O_3$ on AlGaN/GaN MIS-HEMT. *Chin Phys B* **30**, 057302. https://doi.org/10.1088/1674-1056/abd469

Zhou D, Müller-Caspary K, Sigle W, Krause FF, Rosenauer A & van Aken PA (2016). Sample tilt effects on atom column position determination in ABF–STEM imaging. *Ultramicroscopy* **160**, 110–117. https://doi.org/10.1016/j.ultramic.2015.10.008

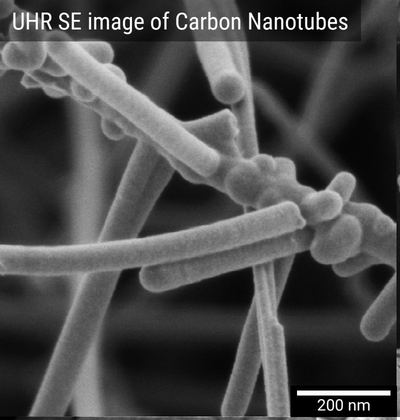
UHR SE image of Carbon Nanotubes

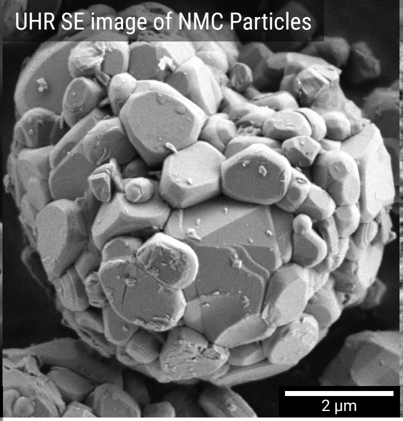
UHR SE image of NMC Particles

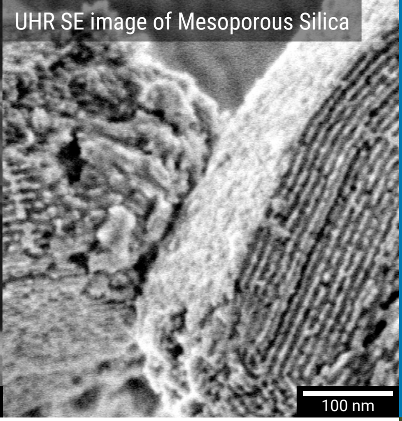
UHR SE image of Mesoporous Silica

Capture surface details at the nanoscale from any materials

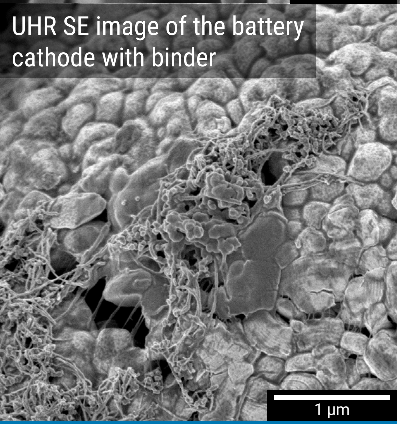
UHR SE image of the battery cathode with binder

NEW GENERATION

TESCAN CLARA

UHR SEM for quick, accurate and comprehensive nanoscale surface analysis of any material

TESCAN


EDS map of the ancient plaster

Reveal new contrast information and hidden features

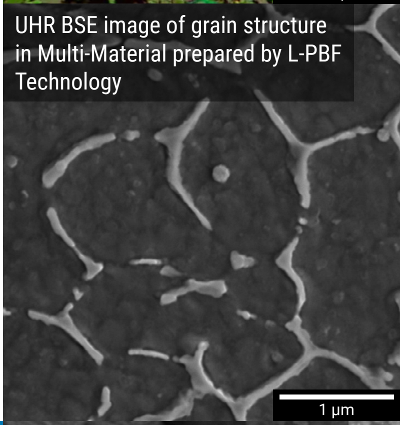
UHR BSE image of grain structure in Multi-Material prepared by L-PBF Technology

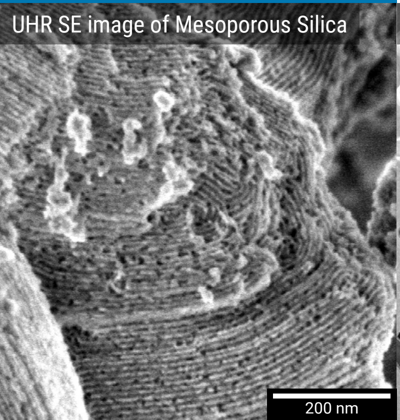
UHR SE image of Mesoporous Silica

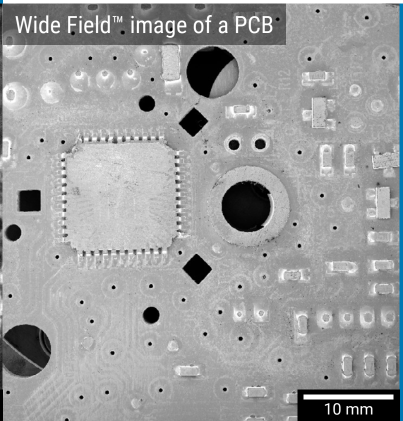
Wide Field™ image of a PCB

Obtain the right data in a short time disregard your SEM experience

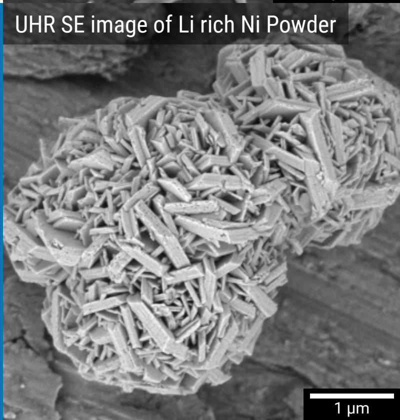
UHR SE image of Li rich Ni Powder